

# High-dimensional density estimation with tensorizing flow

Yinuo Ren<sup>1</sup>

YINUOREN@STANFORD.EDU

Hongli Zhao<sup>2</sup>

HONGLIZHAOBOB@UCHICAGO.EDU

Yuehaw Khoo<sup>2</sup>

YKHOO@UCHICAGO.EDU

Lexing Ying<sup>1,3</sup>

LEXING@STANFORD.EDU

<sup>1</sup>*Institute for Computational and Mathematical Engineering (ICME), Stanford University, Stanford, CA 94305, USA*

<sup>2</sup>*Department of Statistics, University of Chicago, Chicago, IL 60637, USA*

<sup>3</sup>*Department of Mathematics, Stanford University, Stanford, CA 94305, USA*

## Abstract

We propose the tensorizing flow method for estimating high-dimensional probability density functions from the observed data. The method is based on both tensor-train and flow-based generative modeling. Our method first efficiently constructs an approximate density in the tensor-train form via solving the tensor cores from a linear system based on the kernel density estimators of low-dimensional marginals. We then train a continuous-time flow model from this tensor-train density to the observed empirical distribution by performing a maximum likelihood estimation. The proposed method combines the optimization-less feature of the tensor-train with the flexibility of the flow-based generative models. Numerical results are included to demonstrate the performance of the proposed method.

**Keywords:** maximum likelihood estimation, density estimation, tensor-train, flow-based generative modeling

## 1. Introduction

Density estimation is one of the most important tasks of statistics and plays a crucial role in statistical inference, machine learning, and data analysis. It aims to reconstruct the underlying probability density function directly from observed data. The estimation for high-dimensional probability distributions has remained a main challenge both theoretically and computationally.

In recent years, deep generative modeling has been developed as a popular method for approximating high dimensional densities from a large number of samples (Bond-Taylor et al., 2021). Several influential advances in this area include the variational autoencoder (VAE) (Kingma and Welling, 2013) and generative adversarial network (GAN) (Goodfellow et al., 2014). Among them, one particular powerful kind of methods is the flow-based generative models (Dinh et al., 2014; Rezende and Mohamed, 2015), which construct a parameterized flow from a normal distribution to the target distribution. However, confining the source distribution to a normal distribution (or a mixture of Gaussians) can be quite restrictive, especially when dealing with singular or multimodal distributions.

The tensor-train network (Oseledets, 2011), also known as the matrix product state (MPS) (Perez-Garcia et al., 2006) in the physics literature, is a class of tensor network structures widely used to model high-dimensional functions, such as the wavefunction of many-

body quantum states under certain correlation decay assumptions (Brandao and Horodecki, 2015). Inspired by its success in physics, the tensor-train structure has also been applied to many other contexts. Various methods are proposed for efficiently obtaining the tensor-train representation of closed-form high-dimensional functions by the techniques of linear algebra (Oseledets and Tyrtyshnikov, 2010), optimization (Savostyanov and Oseledets, 2011) and parallel computing (Shi et al., 2021). More recently, Hur et al. (2022) proposes an optimization-less linear algebra framework for recovering the tensor-train representation of a density directly from its empirical distribution. However, tensor-trains can be inflexible when it comes to machine learning applications. When working with tensor-train, one needs to pre-determine the ordering of the variables according to their correlations, which may be difficult in practice. A sub-optimal ordering may result in larger ranks of the tensor-train and hence higher storage and computational complexity.

## 1.1 Contributions

Motivated by the strengths as well as the limitations of the flow-based generative models and the tensor-train representation, we propose a new framework that combines the benefits of both approaches for density estimation. More specifically,

- We first construct a low-rank approximate tensor-train representation directly from samples as the base distribution. In particular, in order to deal with the data sparsity in high-dimensional settings, the required low-order marginals during the construction are estimated by the kernel density estimation.
- We then adopt an ODE-based continuous-time flow model that maps the approximate tensor-train distribution to the target distribution. The flow model is parameterized by a neural network and is trained based on the maximum likelihood estimation with both forward and inverse map computed efficiently.

Following the work by Khoo et al. (2022), we refer to this method as the *tensorizing flow* approach for density estimation.

## 1.2 Related works

### DEEP GENERATIVE MODELING

One of the earliest deep generative models is the Boltzmann machine (Hinton and Sejnowski, 1983; Hinton, 2002), which is based on a certain supposed form of the energy function of the probability distribution. The method of VAE (Kingma and Welling, 2013; Rezende et al., 2014) considers an encoding of the observations in a regularized latent space. Other approaches include GAN (Goodfellow et al., 2014), which consists of a generator and a discriminator trained jointly as a minimax game (Schmidhuber, 2020), as well as the autoregressive likelihood models (Bengio et al., 2000; Larochelle and Murray, 2011; Germain et al., 2015), which are based on the chain rule of probability.

Flow-based generative modeling (Dinh et al., 2014; Rezende and Mohamed, 2015) is another deep generative modeling technique based on a sequence of diffeomorphisms between a known base distribution and a target distribution of interest. Unlike the autoregressive models and VAEs, the transformation performed in flow-based models must be invertible

and the determinant of its Jacobian should be computed efficiently (Kobyzev et al., 2020). Several widely-adopted architectures are the planar flow (Rezende and Mohamed, 2015), coupling flow (Dinh et al., 2014, 2016), autoregressive flow (Kingma et al., 2016; Papamakarios et al., 2017),  $1 \times 1$  convolution (Kingma and Dhariwal, 2018), and spline flow (Durkan et al., 2019a,b). Residual networks use residual connections to build a reversible network, as in RevNets (Gomez et al., 2017), iRevNets (Jacobsen et al., 2018), and iResNet (Behrmann et al., 2019).

The idea of residual connections can be generalized to continuous-time or infinitesimal flow models. One type of the continuous-time flow models is formulated by the theory of ordinary differential equations (ODEs) (Chen et al., 2018b; Grathwohl et al., 2018; Dupont et al., 2019), among which Zhang et al. (2018) proposes a continuous-time gradient flow model from the perspective of optimal transport and fluid dynamics. The other type is based on diffusion processes and formulated by stochastic differential equations (SDEs) (Tabak and Vanden-Eijnden, 2010; Chen et al., 2018a; Tzen and Raginsky, 2019).

#### TENSOR-TRAIN REPRESENTATION

The tensor-train representation originates from the density-matrix renormalization group (DMRG) (White, 1993) in physics and plays important roles in computational mathematics (De Lathauwer et al., 2000a,b; Grasedyck, 2010). It sees successful applications in high-dimensional scientific computing problems (Dolgov et al., 2014; Kressner and Uschmajew, 2016; Bachmayr et al., 2016), quantum chemistry and molecular physics (Chan and Sharma, 2011; Baiardi and Reiher, 2020), and signal and image processing (Cichocki et al., 2009; Wang et al., 2018). Many methods have been proposed for constructing the low-rank tensor-train representation of high-dimensional functions in the scenario in which one is able to evaluate the function at arbitrary points or with limited number of evaluations, such as TT-cross (Oseledets and Tyrtshnikov, 2010) and DMRG-cross (Savostyanov and Oseledets, 2011), TT completion (Steinlechner, 2016), and STTA (Kressner et al., 2022).

The tensor-train representation has also been recently applied to generative modeling, in which scenario one constructs the tensor-train model directly from samples without the access to the values of the density function. Several earliest attempts are based on the optimization-based DMRG scheme (Han et al., 2018; Bradley et al., 2020), and Riemannian optimization (Novikov et al., 2021). In the work by Hur et al. (2022), an optimizationless method is proposed for constructing the tensor-train representation directly from samples using a sketching technique. Some other works also manage to take advantage of other structures of tensor networks, including the tree tensor network (Cheng et al., 2019; Tang et al., 2022), and the projected entangled-pair state (PEPS) (Vieijra et al., 2022).

#### VARIATIONAL INFERENCE VIA TENSORIZING FLOW

Density estimation via the maximum likelihood estimation is closely related to the variational inference (VI) problem. Variational inference aims to approximate an unnormalized density with a low-complexity ansatz by solving an optimization problem over variational parameters (Blei et al., 2017). Early approaches include mean-field VI, coordinate ascend VI (Bishop and Nasrabadi, 2006), stochastic VI (Hoffman et al., 2013), and black box VI (Ranganath et al., 2014). Recently, deep neural networks have also been actively ap-

plied in this field (Mnih and Gregor, 2014; Miao et al., 2016). In a manuscript (Khoo et al., 2022), tensorizing flow, *i.e.* the combination of a tensor-based distribution and the neural network, is suggested for variational inference problems, in which an unnormalized analytic form of the density is given for constructing the approximate tensor-train representation. In contrast, our current density estimation task constructs the approximate density only based on limited given samples, and consequently a different set of techniques requires developing so as to deal with the challenges therein.

### 1.3 Organization

The paper is organized as follows. In Section 2, we introduce some preliminaries. Our proposed method is detailed in Section 3. We demonstrate the advantage of our proposed method via numerical experiments in Section 4. Finally we conclude in Section 5 with some discussions of our method.

## 2. Problem and Background

In this section, we introduce the problem setting and the commonly-used notations in Section 2.1, the tensor-train representation for both tensors and general functions in Section 2.2, and the continuous-time flow model in Section 2.3.

### 2.1 Problem setting and notations

We work with probability distributions  $p(\mathbf{x})$  defined on  $\mathbb{R}^d$ , where  $\mathbf{x} = (x_1, \dots, x_d)$  with  $x_i$  as the individual coordinates. Suppose we are given  $N$  independent  $d$ -dimensional samples  $\{\mathbf{x}^{(i)} = (x_1^{(i)}, \dots, x_d^{(i)})\}_{1 \leq i \leq N}$  drawn from an unknown distribution with probability density  $p^*(\mathbf{x}) : \mathbb{R}^d \rightarrow \mathbb{R}$ , the problem is to construct another probability density  $p_\theta(\mathbf{x})$  with parameter  $\theta$  that can serve as an approximation to  $p^*(\mathbf{x})$ . The approximation  $p_\theta(\mathbf{x})$  is also expected to be normalized and easy-to-sample.

Let  $p^E(\mathbf{x})$  be the empirical distribution of the samples, *i.e.*

$$p^E(\mathbf{x}) = \frac{1}{N} \sum_{i=1}^N \delta(\mathbf{x} - \mathbf{x}^{(i)}). \quad (1)$$

This task is typically formulated via the maximum likelihood estimation, where the parameter  $\theta$  is obtained by

$$\begin{aligned} \theta &= \operatorname{argmin}_\theta \operatorname{D}_{\text{KL}}(p^*(\cdot) \| p_\theta(\cdot)) = \operatorname{argmin}_\theta \mathbb{E}_{\mathbf{x} \sim p^*} [-\log p_\theta(\mathbf{x})] \\ &\approx \operatorname{argmin}_\theta \mathbb{E}_{\mathbf{x} \sim p^E} [-\log p_\theta(\mathbf{x})]. \end{aligned} \quad (2)$$

In what follows, we often adopt MATLAB notation in order to simplify the notations. For example,  $m : n$  represents  $m, \dots, n$ . For a 3-tensor  $\mathbf{A}$ ,  $\mathbf{A}(:, i, :)$  denotes the  $i$ -th slice of the 3-dimensional tensor  $\mathbf{A}$  along its second dimension. We also write  $1, \dots, n$  by  $[n]$ , variables  $x_m, \dots, x_n$  by  $x_{m:n}$ , and the corresponding infinitesimal volume  $dx_m \cdots dx_n$  by  $dx_{m:n}$ . For a distribution  $p(\mathbf{x})$ , the marginal distribution of variables  $x_{m:n}$  is denoted by  $p(x_{m:n})$ . Especially, the marginal distributions of variables  $x_{1:2}, x_{1:3}, \dots, x_{d-2:d}, x_{d-1:d}$  are denoted by

$$p_1(x_{1:2}), p_2(x_{1:3}), \dots, p_{d-1}(x_{d-2:d}), p_d(x_{d-1:d}), \quad (3)$$

among which  $p_1$  and  $p_d$  are 2-marginals and the rest are 3-marginals.

For simplicity, we often assume  $p(\mathbf{x})$  to be sufficiently smooth and  $\text{supp}(p) \subset I^d$  for an interval  $I \subset \mathbb{R}$ . In the discussions throughout Sections 2 and 3, we assume  $I = [-1, 1]$  while the general cases where  $I = [a, b]$  or even  $I = \mathbb{R}$  can be handled similarly via appropriate translations and re-scaling.

## 2.2 Tensor-train representation

In modern machine learning and scientific computing, data are often presented as tensors. A  $d$ -dimensional tensor  $\mathbf{F}$  in  $\mathbb{R}^{n \times \dots \times n}$  is a collection of numbers denoted by  $\mathbf{F}(i_1, \dots, i_d)$  with  $1 \leq i_1, \dots, i_d \leq n$ . It has  $n^d$  elements and is generally impractical to handle due to its exponential computational cost as the dimension  $d$  grows.

One way to represent or approximate high-dimensional tensors is to use the *tensor-train (TT) representation*, *i.e.*

$$\mathbf{F}(i_1, \dots, i_d) \approx \mathbf{G}_1(i_1, :) \mathbf{G}_2(:, i_2, :) \cdots \mathbf{G}_d(:, i_d), \quad (4)$$

where  $\mathbf{G}_1 \in \mathbb{R}^{n \times r_1}$ ,  $\mathbf{G}_2 \in \mathbb{R}^{r_1 \times n \times r_2}$ ,  $\dots$ ,  $\mathbf{G}_d \in \mathbb{R}^{r_{d-1} \times n}$  are the *cores*, and  $r_i$  for  $1 \leq i \leq d-1$  are the *ranks* of the TT representation.

The tensor  $\mathbf{F}$  is then represented by the product of a sequence of corresponding slices of the cores, which is often described in the *diagrammatic notation* as shown in Figure 1a. We refer the readers to the discussions by Penrose (1971) for the interpretation of this kind of notations. When the ranks  $\{r_i\}_{1 \leq i \leq d-1}$  are bounded, TT format features linear cost in  $n$  and  $d$ .

The idea of tensor-train can also be generalized to obtain the low-rank approximation of high-dimensional functions. The TT representation of a general  $d$ -dimensional function  $F(\mathbf{x}) : I^d \rightarrow \mathbb{R}$  is comprised of a sequence of  $d$  functions  $G_1 : I \times [r_1] \rightarrow \mathbb{R}$ ,  $G_2 : [r_1] \times I \times [r_2] \rightarrow \mathbb{R}$ ,  $\dots$ ,  $G_d : [r_{d-1}] \times I \rightarrow \mathbb{R}$ , as

$$F(x_{1:d}) \approx \sum_{\alpha_1=1}^{r_1} \sum_{\alpha_2=1}^{r_2} \cdots \sum_{\alpha_{d-1}=1}^{r_{d-1}} G_1(x_1, \alpha_1) G_2(\alpha_1, x_2, \alpha_2) \cdots G_d(\alpha_{d-1}, x_d), \quad (5)$$

or more compactly

$$F(x_{1:d}) \approx G_1(x_1, :) G_2(:, x_2, :) \cdots G_d(:, x_d).$$

The diagrammatic notation of this continuous tensor-train is shown in Figure 1b.

## 2.3 Continuous-time flow model

Typically, a flow-based generative model aims to design a pushforward  $f : \mathbb{R}^d \rightarrow \mathbb{R}^d$  between a latent easy-to-sample probability density  $q_0(\mathbf{x})$  and a challenging target probability density  $q_1(\mathbf{x})$  that satisfies

$$q_1(\mathbf{x}) = q_0(f^{-1}(\mathbf{x})) \left| \det \left( \frac{\partial f^{-1}}{\partial \mathbf{x}} \right) \right|. \quad (6)$$

A *continuous-time flow model* is based on the perspective that regards  $f$  as the result of a flow that pushes the density  $q(\mathbf{x}, t)$  initialized as  $q(\mathbf{x}, 0) = q_0(\mathbf{x})$  over time  $t$  with total

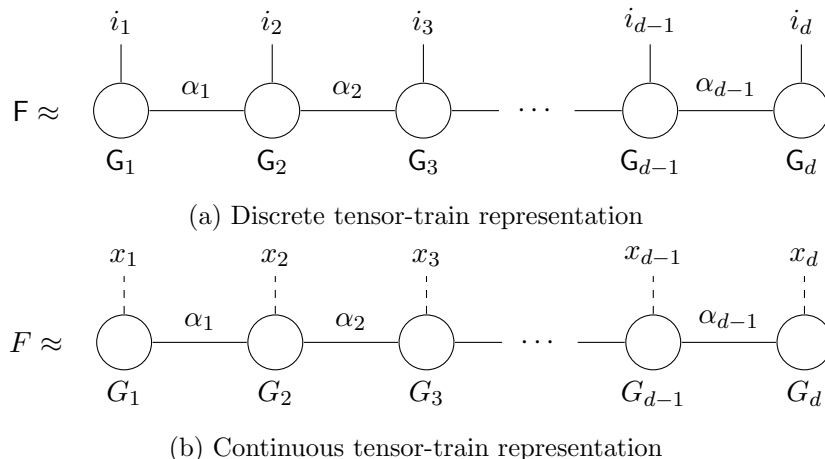


Figure 1: The diagrammatic notation of the tensor-train representation: Solid lines represent discrete indices while dashed lines represent continuous variables.

probability mass being conserved. The evolution of the density  $q(\mathbf{x}, t)$  is characterized by the following *continuity equation* in the fluid mechanics:

$$\frac{\partial q(\mathbf{x}, t)}{\partial t} + \nabla \cdot [q(\mathbf{x}, t)\mathbf{v}(\mathbf{x})] = 0, \quad (7)$$

where  $\mathbf{v}(\mathbf{x})$  is the velocity field of the flow. Motivated by the linearized optimal transport, Zhang et al. (2018) assumes that the flow is irrotational so that  $\nabla \times \mathbf{v}(\mathbf{x}) = 0$ , and consequently  $\mathbf{v}(\mathbf{x})$  can be written as the gradient of a potential function  $\phi(x)$ , *i.e.*  $\mathbf{v}(\mathbf{x}) = \nabla\phi(\mathbf{x})$  (Batchelor, 2000).

An equivalent description concerns the trajectory  $\mathbf{x}(t)$  that follows the velocity field  $\nabla\phi(\mathbf{x})$ , along which the following two ODEs hold:

$$\frac{d\mathbf{x}(t)}{dt} = \nabla\phi(\mathbf{x}(t)), \quad (8a)$$

$$\frac{dq(\mathbf{x}(t), t)}{dt} = -q(\mathbf{x}(t), t)\nabla^2\phi(\mathbf{x}(t)) \quad (8b)$$

where the second equation directly follows from the continuity equation (7) and the formula of total derivative  $d/dt = \partial/\partial t + d\mathbf{x}(t)/dt \cdot \nabla$  (Batchelor, 2000). This formulation provides a more straightforward way to understand the forward map  $f$  as the map from  $\mathbf{x}(0)$  to  $\mathbf{x}(T)$  and the inverse map  $f^{-1}$  as that from  $\mathbf{x}(T)$  to  $\mathbf{x}(0)$ . In the implementation, the dynamic system (8) is realized by the fourth order Runge-Kutta scheme with a sufficiently small stepsize  $\tau$ . During the evaluation of  $q(\mathbf{y}, T)$  for an arbitrary  $\mathbf{y}$ , we first compute the inverse map  $f^{-1}(\mathbf{y})$  by solving (8a) from  $t = T$  to 0 with  $\mathbf{x}(T) = \mathbf{y}$ , and then solve (8b) from  $t = 0$  to  $T$  with  $q(\mathbf{x}(0), 0) = p_0(f^{-1}(\mathbf{y}))$ . During sampling, we first draw a sample  $\mathbf{y}$  from the initial distribution  $p_0$  and then output  $f(\mathbf{y})$  by solving (8a) from  $t = 0$  to  $T$  with  $\mathbf{x}(0) = \mathbf{y}$ .

For a predetermined time horizon  $T$ , the flow guided by different potential functions  $\phi(\mathbf{x})$  may evolve the initial density  $q(\mathbf{x}, 0) = q_0(\mathbf{x})$  into a variety of densities  $q(\mathbf{x}, T)$  at time  $T$ . From the perspective of optimal control theory, the optimal potential function

$\phi(\mathbf{x})$  for approximating the target density  $q_1(\mathbf{x})$  should be the solution to the following optimization problem:

$$\min_{\phi: \mathbb{R}^d \rightarrow \mathbb{R}} D(q_1(\cdot), q(\cdot, T)), \quad (9)$$

where  $D(\cdot, \cdot)$  is a proper metric or divergence for probability measures.

The potential function  $\phi(\mathbf{x})$  is parameterized by a neural network denoted as  $\phi_\theta(\mathbf{x})$  with parameter  $\theta$ . In what follows, we shall denote the resulting pushforward  $f$  and density  $q(\mathbf{x}, T)$  by this continuous-time flow model as  $f_\theta$  and  $q_\theta(\mathbf{x})$ . Taking the metric  $D(\cdot, \cdot)$  in (9) as the Kullback-Leibler (KL) divergence, (9) amounts to an MLE as in (2) and the parameter  $\theta$  of the neural network is thus trained by minimizing over the negative log-likelihood

$$\theta = \operatorname{argmin}_\theta \mathbb{E}_{\mathbf{x} \sim q_1} \left[ \log \frac{q_1(\mathbf{x})}{q_\theta(\mathbf{x})} \right] = \operatorname{argmin}_\theta \mathbb{E}_{\mathbf{x} \sim q_1} [-\log q_\theta(\mathbf{x})].$$

The mechanism of this continuous-time flow model is shown in Figure 2.

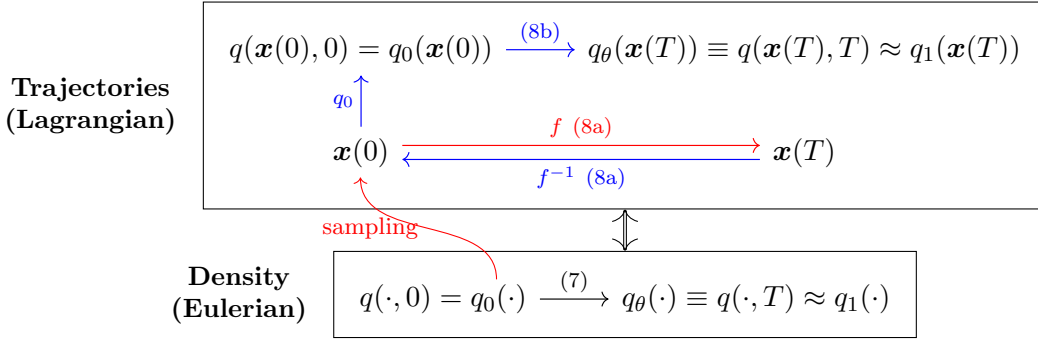


Figure 2: The mechanism of the continuous-time flow model: the blue path shows the evaluation procedure and the red arrow shows the sampling procedure for the resulting density  $q_\theta(\cdot)$ .

### 3. Tensorizing flow

This section presents our tensorizing flow algorithm for high-dimensional density estimation. As an overview, the algorithm consists of two main steps:

$$p^{\text{E}(\cdot)} = \frac{1}{N} \sum_{i=1}^N \delta(\cdot - \mathbf{x}^{(i)}) \xrightarrow{1} p^{\text{TT}(\cdot)} \xrightarrow{2} p^{\text{TF}(\cdot)}$$

1. Construct an approximate tensor-train representation  $p^{\text{TT}}$  from the samples  $\{\mathbf{x}^{(i)}\}_{1 \leq i \leq N}$  by combining sketching techniques with kernel density estimation (Section 3.1);
2. Apply the continuous-time flow model to drive  $p^{\text{TT}}$  towards  $\{\mathbf{x}^{(i)}\}_{1 \leq i \leq N}$ , with the resulting distribution denoted by  $p^{\text{TF}}$  (Section 3.2).

#### 3.1 Construction of $p^{\text{TT}}$

We start with a conceptual algorithm and follow by a more practical one.

### 3.1.1 IDEAL CASE

Let us motivate the construction of an approximate TT representation by considering an ideal case where the underlying density  $p$  has a *finite-rank* structure and is also *Markovian*, which are explained as follows.

We assume that all reshaped versions  $p(x_{1:k}; x_{k+1:d})$  of  $p(\mathbf{x})$  for  $1 \leq k \leq d-1$  are Hilbert-Schmidt kernels (Stein and Shakarchi, 2009) so that we can apply singular value decomposition (SVD) (Young, 1988) (also called Schmidt decomposition) to them. For a Hilbert-Schmidt kernel  $K$ , we define its *column space* by its range, and its *row space* by the range of its adjoint.

**Definition 1 (Finite-rank)** *A probability density function  $p(\mathbf{x})$  is finite-rank if for any  $1 \leq k \leq d-1$ , the reshaped version  $p(x_{1:k}; x_{k+1:d})$  of  $p(\mathbf{x})$  as a Hilbert-Schmidt kernel is finite-rank, i.e. of finite-dimensional column space.*

We also assume throughout that all the marginal distributions of  $p(\mathbf{x})$ , especially the 2 or 3-marginals  $p_k$  (3), belong to the class of Hilbert-Schmidt kernels so we can also perform SVD to them when necessary.

**Definition 2 (Markovian)** *A probability density function  $p(\mathbf{x})$  is Markovian if it can be written in*

$$p(\mathbf{x}) = p(x_1)p(x_2|x_1) \cdots p(x_d|x_{d-1}).$$

**Finite-rank structure** Under the finite-rank assumption, the cores of the TT representation of  $p(\mathbf{x})$  can be obtained simply via the following proposition:

**Proposition 3 (Core determining equation)** *Suppose that the probability density  $p$  is finite-rank. For  $1 \leq k \leq d-1$ , denote the rank of its reshaped version  $p(x_{1:k}; x_{k+1:d})$  by  $r_k$  and let  $\{\Phi_k(x_{1:k}; \alpha_k)\}_{1 \leq \alpha_k \leq r_k}$  be the first  $r_k$  left singular vectors of  $p(x_{1:k}; x_{k+1:d})$ . Then there exists a unique solution  $G_1 : I \times [r_1] \rightarrow \mathbb{R}, G_2 : [r_1] \times I \times [r_2] \rightarrow \mathbb{R}, \dots, G_d : [r_{d-1}] \times I \rightarrow \mathbb{R}$  to the following system of core determining equations (CDEs):*

$$\begin{aligned} G_1(x_1; \alpha_1) &= \Phi_1(x_1; \alpha_1), \\ \sum_{\alpha_{k-1}=1}^{r_{k-1}} \Phi_{k-1}(x_{1:k-1}; \alpha_{k-1}) G_k(\alpha_{k-1}; x_k, \alpha_k) &= \Phi_k(x_{1:k-1}; x_k, \alpha_k), \quad 2 \leq k \leq d-1, \\ \sum_{\alpha_{d-1}=1}^{r_{d-1}} \Phi_{d-1}(x_{1:d-1}; \alpha_{d-1}) G_d(\alpha_{d-1}; x_d) &= p(x_{1:d-1}; x_d), \end{aligned} \tag{10}$$

where the cores  $G_k$  give an exact TT representation of  $p(\mathbf{x})$ :

$$p(\mathbf{x}) = G_1(x_1, \cdot) G_2(\cdot, x_2, \cdot) \cdots G_d(\cdot, x_d). \tag{11}$$

We refer to Appendix A for the proof of this proposition.



**Left-sketching technique** Unfortunately, the size of equations in (10) grows exponentially with the dimension  $d$  (even after discretization) and consequently it is impossible to estimate all the coefficients  $\Phi_k$  from finite samples. A key observation is that this linear system is significantly over-determined so it can be reduced efficiently by a sketching technique. To implement the sketching, we select suitable left-sketching functions  $S_{k-1}(y_{k-1}; x_{1:k-1})$  for  $2 \leq k \leq d$ , where  $y_{k-1} \in \mathcal{Y}_{k-1}$  with  $\mathcal{Y}_{k-1}$  being an appropriate set specified by the model. By contracting them with the left-hand sides of (10), we obtain the following reduced system of CDEs:

$$\begin{aligned}
 G_1(x_1; \alpha_1) &= B_1(x_1; \alpha_1), \\
 \sum_{\alpha_{k-1}=1}^{r_{k-1}} A_{k-1}(y_{k-1}; \alpha_{k-1}) G_k(\alpha_{k-1}; x_k, \alpha_k) &= B_k(y_{k-1}; x_k, \alpha_k), \quad 2 \leq k \leq d-1, \\
 \sum_{\alpha_{d-1}=1}^{r_{d-1}} A_{d-1}(y_{d-1}; \alpha_{d-1}) G_d(\alpha_{d-1}; x_d) &= B_d(y_{d-1}; x_d),
 \end{aligned} \tag{12}$$

where the coefficients  $B_k$  and  $A_k$  are given by

$$\begin{aligned}
 B_1(x_1; \alpha_1) &= \Phi_1(x_1; \alpha_1), \\
 B_k(y_{k-1}; x_k, \alpha_k) &= \int_{I^{k-1}} S_{k-1}(y_{k-1}; x_{1:k-1}) \Phi_k(x_{1:k-1}; x_k, \alpha_k) dx_{1:k-1}, \quad 2 \leq k \leq d-1 \\
 B_d(y_{d-1}; x_d) &= \int_{I^{d-1}} S_{d-1}(y_{d-1}; x_{1:d-1}) p(x_{1:d-1}; x_d) dx_{1:d-1}, \\
 A_{k-1}(y_{k-1}; \alpha_{k-1}) &= \int_{I^{k-1}} S_{k-1}(y_{k-1}; x_{1:k-1}) \Phi_{k-1}(x_{1:k-1}; \alpha_{k-1}) dx_{1:k-1}, \quad 2 \leq k \leq d.
 \end{aligned} \tag{13}$$

Generally, the left-sketching functions  $S_{k-1}(y_{k-1}; x_{1:k-1})$  need to be chosen such that the row space of  $\Phi_k(x_{1:k-1}; x_k, \alpha_k)$  is retained and the variance of the coefficient matrices is reduced as much as possible (Hur et al., 2022). For an illustration of the sketching technique, we refer readers to Figure 3 for the diagrammatic notation of the  $k$ -th equation in the reduced CDEs (12) for  $2 \leq k \leq d-1$  (*cf.* the corresponding equation in the original CDEs (10)).

**Markovian structure** In general, it is unclear what  $S_k$  one needs to choose in order to obtain  $B_k$  and  $A_k$  in (13). Furthermore, in practice it is impossible to compute or estimate the singular vectors  $\Phi_k$  involved. However, under the extra Markovian assumption, the computation for  $B_k$  and  $A_k$  can be made simple due to the following lemma:

**Lemma 4 (Hur et al. (2022, Lemma 5))** *Suppose  $p(\mathbf{x})$  is Markovian, then for any  $i \leq k \leq j-1$ ,*

1.  $p(x_{i:k}; x_{k+1:j})$  and  $p(x_{i:k}; x_{k+1})$  have the same column space;
2.  $p(x_{i:k}; x_{k+1:j})$  and  $p(x_k; x_{k+1:j})$  have the same row space.

Lemma 4 essentially tells us that for  $p(x_{1:k}; x_{k+1:d})$ , marginalizing out  $x_{k+2:d}$  or  $x_{1:k-1}$  will not affect the corresponding column or row space. Motivated by this lemma, we are able to make the following two simplifications when computing the coefficients  $B_k$  and  $A_k$  in (10):

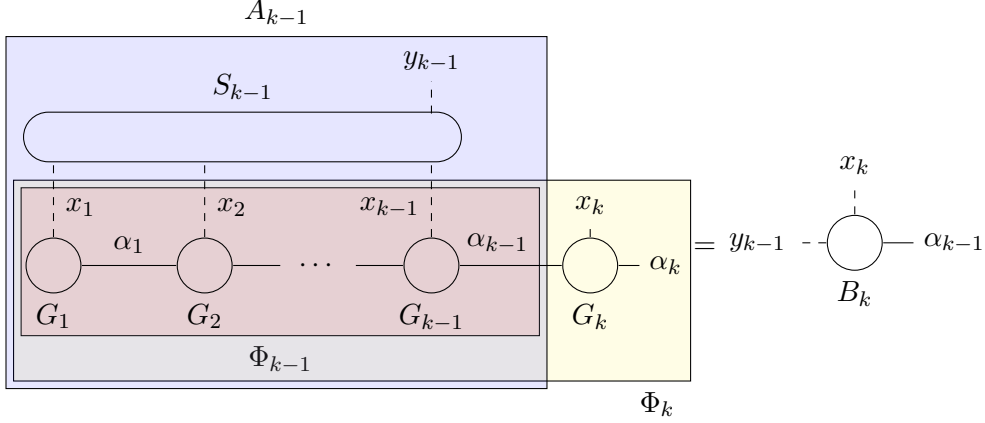


Figure 3: The diagrammatic notation of the  $k$ -th equation in the reduced CDEs (12) for  $2 \leq k \leq d-1$  (cf. the corresponding equation in the original CDEs (10)).

1. Obtain  $\Phi_k(x_{1:k}; \alpha_k)$  for  $1 \leq k \leq d-1$  by only considering the column space of the  $(k+1)$ -dimensional marginal distribution  $p(x_{1:k}; x_{k+1})$  instead of the full distribution  $p(x_{1:k}; x_{k+1:d})$ ;
2. Simply take  $\mathcal{Y}_{k-1} = I$  and  $S_{k-1}(y_{k-1}; x_{1:k-1}) = \delta(y_{k-1} - x_{k-1})$ , i.e. the Schwartz distribution that marginalizes out the first  $k-2$  dimensions, for  $2 \leq k \leq d$  as suggested by Hur et al. (2022).

For  $k=1$ , these simplifications indicate that  $\Phi_1(x_1; \alpha_1)$  can be obtained directly by applying SVD to the 2-marginal  $p_1(x_1; x_2)$ , and subsequently

$$A_1(y_1; \alpha_1) = \int_I \delta(y_1 - x_1) \Phi_1(x_1; \alpha_1) dx_1 = \Phi_1(y_1; \alpha_1) = B_1(y_1; \alpha_1),$$

where the last equality is by definition (13). Similarly, for  $k=d$ ,  $B_d(y_{d-1}; x_d) = p_d(y_{d-1}; x_d)$ .

For  $2 \leq k \leq d-1$ , the simplifications yield

$$\begin{aligned} B_k(y_{k-1}; x_k, \alpha_k) &= \int_{I^{k-1}} \delta(y_{k-1} - x_{k-1}) \Phi_k(x_{1:k-1}; x_k, \alpha_k) dx_{1:k-1} \\ &= \int_{I^{k-2}} \Phi_k(x_{1:k-2}; y_{k-1}, x_k, \alpha_k) dx_{1:k-2}. \end{aligned} \quad (14)$$

A natural way to obtain  $B_k$  is to first calculate  $\Phi_k(x_{1:k}; \alpha_k)$  by performing SVD directly to  $p(x_{1:k}; x_{k+1})$  and apply left-sketching afterwards, i.e. marginalizing out  $x_{1:k-2}$  from  $\Phi_k(x_{1:k}; \alpha_k)$  as in (14). However, this approach is practically infeasible, since  $p(x_{1:k}; x_{k+1})$  is again exponentially large to  $d$  and its range  $\Phi_k(x_{1:k}; \alpha_k)$  can hardly be estimated by a limited collection of samples. Thus instead, we obtain  $B_k$  in an implicit manner by first applying the left-sketching functions  $S_{k-1}$  to  $p(x_{1:k}; x_{k+1})$ , i.e. marginalizing out  $x_{1:k-2}$  from  $p(x_{1:k}; x_{k+1})$  to obtain the 3-marginal  $p_k(x_{k-1}, x_k; x_{k+1})$ , and then performing SVD to  $p_k(x_{k-1}, x_k; x_{k+1})$ . Then  $B_k(x_{k-1}, x_k; \alpha_k)$  is formed by the first  $r_k$  left singular vectors

of  $p_k(x_{k-1}, x_k; x_{k+1})$ . Moreover, since

$$\begin{aligned} A_k(y_k; \alpha_k) &= \int_{I^k} \delta(y_k - x_k) \Phi_k(x_{1:k}; \alpha_k) dx_{1:k} = \int_{I^{k-1}} \Phi_k(x_{1:k-1}; y_k, \alpha_k) dx_{1:k-1} \\ &= \int_I \int_{I^{k-2}} \Phi_k(x_{1:k-2}; y_{k-1}, y_k, \alpha_k) dx_{1:k-2} dy_{k-1} = \int_I B_k(y_{k-1}; y_k, \alpha_k) dy_{k-1}, \end{aligned}$$

$A_k$  is obtained subsequently by marginalizing out the first dimension of  $B_k$ .

In conclusion, we are able to obtain an exact TT representation in the form of (11) for the finite-rank and Markovian distributions  $p(\mathbf{x})$  by first forming the coefficients  $B_k$  and  $A_k$  and then solving the reduced system of CDEs (12).

### 3.1.2 GENERAL CASE

The ideal case in Section 3.1.1 assumes that the distribution  $p$  is finite-rank and Markovian. It also assumes the function access to the marginals  $p_k$  (3) and the singular value decomposition for Hilbert-Schmidt kernels (rather than finite-dimensional matrices). In practice, we need to deal with an unknown underlying distribution  $p^*$ , which is not necessarily low-rank and Markovian. Furthermore, instead of the analytic formulae of the marginals, we only have access to a limited set of samples  $\{\mathbf{x}^{(i)}\}_{1 \leq i \leq N}$  drawn from the unknown  $p^*$ .

In order to bridge this gap between the ideal case and the practical situation, we describe below how to adapt the method described in Section 3.1.1. The resulting TT  $p^{\text{TT}}$  will serve as a reasonable approximation to the unknown underlying distribution  $p^*$ .

**Step 1.** Construct the kernel density estimators  $p_k^{\text{S}}$  of the marginals  $p_k^*$  (3) from the samples  $\{\mathbf{x}^{(i)}\}_{1 \leq i \leq N}$  for  $1 \leq k \leq d$ .

When evaluating the coefficients  $B_k$  and  $A_k$ , the most direct approach is to estimate the marginals  $p_k^*$  by directly interpolating the marginal distribution  $p_k^{\text{E}}$  of the empirical distribution  $p^{\text{E}}$  (1) with polynomials as in the work by Hur et al. (2022). Instead, we estimate  $p_k^*$  by applying kernel density estimation (KDE) to the corresponding slices of samples, *e.g.* for  $2 \leq k \leq d-1$ ,  $p_k^*$  is estimated by the kernel density estimators

$$p_k^{\text{S}}(x_{k-1:k+1}) := \frac{1}{Nh} \sum_{i=1}^N K\left(\frac{x_{k-1:k+1} - x_{k-1:k+1}^{(i)}}{h}\right),$$

where  $K(\cdot)$  is the Gaussian kernel  $(2\pi)^{-3/2} \exp(-\|\cdot\|^2/2)$  and  $h$  is the bandwidth.

**Remark 5** *The adoption of KDE to marginal distributions is key to the construction of the TT representation in practice. The reason is that if we perform SVD directly to the marginal empirical distributions  $p_k^{\text{E}}$ , the sparsity of samples may lead to severe Gibbs phenomenon in the resulting approximate TT representation, posing a major obstacle in the way of implementing tensorizing flow. Therefore,  $p_k^{\text{E}}$  are first smoothed by KDE and SVD is performed to the kernel density estimators  $p_k^{\text{S}}$  instead of  $p_k^{\text{E}}$ . It is also noteworthy that KDE is performed only for estimating the 2 or 3-marginals  $p_k^*$  but not the full distribution  $p^*$ , for applying KDE directly to  $p^*$  would lead to poor performance because of the curse of dimensionality.*

In general, there is a bias-variance trade-off for choosing the bandwidth parameter  $h$ . Specifically, when  $h \rightarrow 0$ , the kernel density estimator  $\hat{p}_k$  approaches the empirical distribution  $p_k^E$ , an unbiased estimator of the true distribution  $p_k$ . As the bandwidth  $h$  grows,  $\hat{p}_k$  becomes smoother with certain bias. When the bandwidth  $h$  is sufficiently large,  $\hat{p}_k$  is smooth enough to be well approximated by polynomial approximation.

**Step 2.** Estimate the coefficients  $B_k$  for  $1 \leq k \leq d$  and  $A_k$  for  $1 \leq k \leq d-1$  from the kernel density estimators  $p_k^S$ .

Ideally,  $B_d = p_d^S$  and for  $1 \leq k \leq d-1$ ,  $B_k$  is formed by the first  $r_k$  left singular vectors by performing SVD to the  $d-1$  kernel density estimators

$$p_1^S(x_1; x_2), p_2^S(x_1, x_2; x_3), \dots, p_{d-1}^S(x_{d-2}, x_{d-1}; x_d).$$

Afterwards,  $A_1 = B_1$ , and  $A_k$  is obtained by marginalizing out the first variable of  $B_k$  for  $2 \leq k \leq d-1$ .

However, since  $x_i$  takes value in  $I = [-1, 1]$  and all marginals are continuous functions, numerical approximation is needed for carrying out SVD practically. To this end, we introduce the normalized Legendre polynomials  $\{L_i(x)\}_{i \geq 1}$  with  $\deg(L_i) = i-1$ , which form an orthonormal basis of  $L^2(I)$ . For example, when evaluating  $B_k$  for  $2 \leq k \leq d-1$ , we take the tensor-product normalized Legendre polynomials  $\{L_{i_{k-1}}(x_{k-1})L_{i_k}(x_k)\}_{1 \leq i_{k-1}, i_k \leq M}$  as the expansion basis for variables  $(x_{k-1}, x_k)$  and  $\{L_{i_{k+1}}(x_{k+1})\}_{1 \leq i_{k+1} \leq M}$  for  $x_{k+1}$ . Here  $M$  is a constant that controls the accuracy of the polynomial approximation. Projecting  $p_k^S(x_{k-1}, x_k; x_{k+1})$  orthogonally onto these two sets of basis functions gives the following  $M^2 \times M$  coefficient matrix with entry

$$\begin{aligned} & P_k^S(i_{k-1}, i_k; i_{k+1}) \\ &= \int_{I \times I} \int_I (L_{i_{k-1}}(x_{k-1})L_{i_k}(x_k)) p_k^S(x_{k-1}, x_k; x_{k+1}) L_{i_{k+1}}(x_{k+1}) dx_{k-1} dx_k dx_{k+1}. \end{aligned}$$

Next, one computes the truncated SVD for  $P_k^S(i_{k-1}, i_k; i_{k+1})$  and groups the first  $r_k$  singular vectors into a matrix  $B_k(i_{k-1}, i_k; \alpha_k)$  of size  $M^2 \times r_k$ , where  $r_k$  is the numerical rank. Finally,  $B_k(x_{k-1}, x_k; \alpha_k)$  can be obtained by

$$B_k(x_{k-1}, x_k; \alpha_k) := \sum_{i_{k-1}=1}^M \sum_{i_k=1}^M B_k(i_{k-1}, i_k; \alpha_k) L_{i_{k-1}}(x_{k-1}) L_{i_k}(x_k),$$

and by contracting  $L_1(x_{k-1}) \equiv 1/\sqrt{2}$  to both sides,  $A_k$  is obtained subsequently by

$$A_k(x_k; \alpha_k) := \sqrt{2} \sum_{i_k=1}^M B_k(1, i_k; \alpha_k) L_{i_k}(x_k).$$

The cases for  $k=1$  and  $d$  are handled similarly.

**Step 3.** Solve (12) by least squares for the cores  $G_1, \dots, G_d$ .

Similar to the previous step, since (12) is formulated in terms of functions, numerical approximation is needed. We again resort to polynomial approximation and expand  $G_k$ ,

$B_k$ , and  $A_k$  w.r.t. the first  $M$  normalized Legendre polynomials, *e.g.* for  $2 \leq k \leq d-1$ , the corresponding coefficient matrices  $G_k$ ,  $B_k$ , and  $A_k$  are given by

$$\begin{aligned} G_k(\alpha_{k-1}; i_k, \alpha_k) &= \int_I G_k(\alpha_{k-1}; x_k, \alpha_k) L_{i_k}(x_k) dx_k, \\ B_k(\beta_{k-1}; i_k, \alpha_k) &= \int_{I \times I} B_k(y_{k-1}; x_k, \alpha_k) L_{\beta_{k-1}}(y_{k-1}) L_{i_k}(x_k) dy_{k-1} dx_k \\ A_{k-1}(\beta_{k-1}; \alpha_{k-1}) &= \int_I A_{k-1}(y_{k-1}; \alpha_{k-1}) L_{\beta_{k-1}}(y_{k-1}) dy_{k-1}. \end{aligned}$$

As interpreted by diagrammatic notation in Figure 4, the projected version of the system (12) is

$$\begin{aligned} G_1(i_1; \alpha_1) &= B_1(i_1; \alpha_1), \\ \sum_{\alpha_{k-1}=1}^{r_{k-1}} A_{k-1}(\beta_{k-1}; \alpha_{k-1}) G_k(\alpha_{k-1}; i_k, \alpha_k) &= B_k(\beta_{k-1}; i_k, \alpha_k), \quad 2 \leq k \leq d-1, \\ \sum_{\alpha_{d-1}=1}^{r_{d-1}} A_{d-1}(\beta_{d-1}; \alpha_{d-1}) G_d(\alpha_{d-1}; i_d) &= B_d(\beta_{d-1}; i_d). \end{aligned} \tag{15}$$

The discrete cores  $G_k$  can be solved efficiently from these equations by applying least squares. Once  $G_k$  are solved, they are combined with the normalized Legendre polynomials to produce the continuous cores

$$G_k(\alpha_{k-1}; x_k, \alpha_k) \approx \sum_{i_k=1}^M G_k(\alpha_{k-1}; i_k, \alpha_k) L_{i_k}(x_k).$$

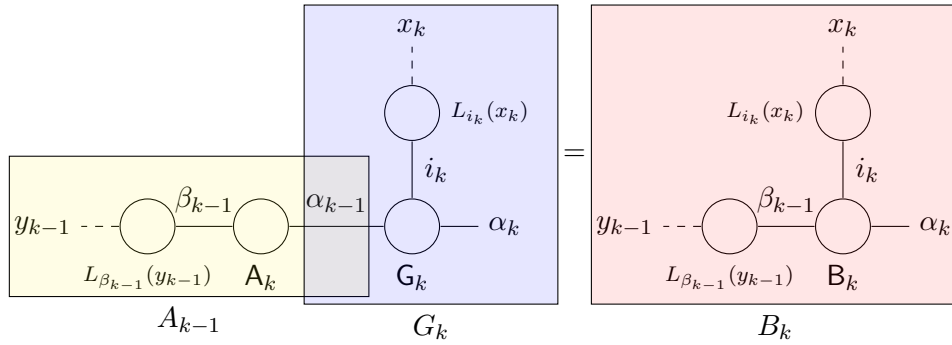


Figure 4: The diagrammatic notation of the  $k$ -th equation in the discrete CDEs (15) for  $2 \leq k \leq d-1$  (*cf.* the corresponding equation in the reduced CDEs (12)).

**Step 4.** With the cores  $G_k$  ready, the approximate TT representation  $p^{\text{TT}}(\mathbf{x})$  of  $p^{\text{E}}(\mathbf{x})$  can be set to  $G_1(x_1, \cdot) G_2(\cdot, x_2, \cdot) \cdots G_d(\cdot, x_d)$  as in (11). However, there are two extra issues to be addressed.

First,  $G_1(x_1, : )G_2(:, x_2, : ) \cdots G_d(:, x_d)$  does not necessarily integrate to unity. The normalization can be done by contracting  $G_1(x_1, : )G_2(:, x_2, : ) \cdots G_d(:, x_d)$  with the all-one function and absorbing the resulting constant into any of  $G_k$  s.t.  $p^{\text{TT}}$  retains the form

$$p^{\text{TT}}(x_{1:d}) := G_1(x_1, : )G_2(:, x_2, : ) \cdots G_d(:, x_d), \quad (16)$$

the diagrammatic notation of which is shown in Figure 5.

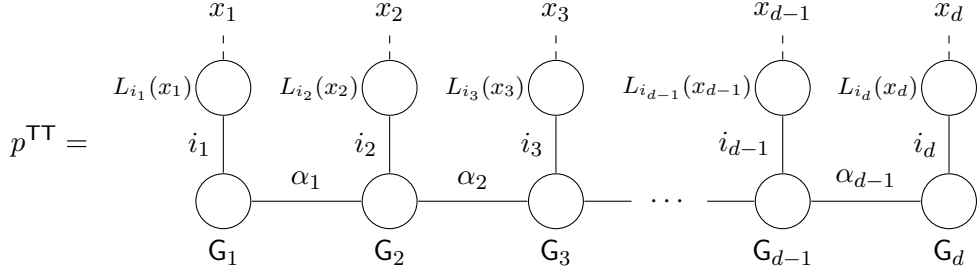


Figure 5: The diagrammatic notation of the approximate TT representation  $p^{\text{TT}}$ .

The second issue is that  $G_1(x_1, : )G_2(:, x_2, : ) \cdots G_d(:, x_d)$  is not necessarily non-negative. To ensure the non-negativity, we can adopt the following post-processing by following the approach of *Born machine* (Han et al., 2018), *i.e.* one solves

$$\begin{aligned} & \min_{q(\mathbf{x})} \left\| p^{\text{TT}}(\mathbf{x}) - r(\mathbf{x})^2 \right\|_{L^2(I^d)} \\ \text{s.t. } & r(\mathbf{x}) = \sum_{i_1=1}^M \cdots \sum_{i_d=1}^M \mathbf{R}(i_{1:M}) L_{i_1}(x_1) \cdots L_{i_d}(x_d), \end{aligned}$$

where  $\mathbf{R}(i_{1:d}) = \mathbf{H}_1(i_1, : )\mathbf{H}_2(:, i_2, : ) \cdots \mathbf{H}_d(:, i_d)$  is a discrete tensor-train with discrete cores  $\mathbf{H}_i$ . Noticing that

$$\int_{I^d} p^{\text{TT}}(\mathbf{x}) d\mathbf{x} = \int_{I^d} r(\mathbf{x})^2 d\mathbf{x} = \|\mathbf{R}\|_F^2$$

by the orthogonality of Legendre polynomials, then

$$p^{\text{TT}}(\mathbf{x}) := r(\mathbf{x})^2 \quad (17)$$

is guaranteed to be non-negative and integrate to one by normalizing the Frobenius norm of the discrete tensor-train  $\mathbf{Q}$ . Strictly speaking, this is not a TT representation, rather the pointwise square of a TT representation.

### 3.2 Construction of $p^{\text{TF}}$

In the second step of our method, instead of using the normal distribution as the base distribution in normalizing flow, we start from the approximate TT representation  $p^{\text{TT}}(\mathbf{x})$  obtained in (16) or (17) and use the continuous-time flow model in Section 2.3 to improve this approximation.

Following Section 2.3, we choose the initial distribution  $q(\mathbf{x}, 0) = p^{\text{TT}}(\mathbf{x})$ , and then select a proper time horizon  $T$  and stepsize  $\tau$  to obtain a new density approximation

$q_\theta(\mathbf{x}) \equiv q(\mathbf{x}, T)$ , where the subscript  $\theta$  indicates the neural network used to parameterize the potential function  $\phi_\theta(\mathbf{x})$  that guides the flow (8).

As in the MLE setup (2), the loss function for training is chosen as the negative log-likelihood:

$$\mathcal{L}(\theta) := -\mathbb{E}_{\mathbf{x} \sim p^E} \log q_\theta(\mathbf{x}). \quad (18)$$

In the actual implementation, the neural network is trained on batches. Each batch is randomly selected from the full sample set  $\{\mathbf{x}^{(i)}\}_{1 \leq i \leq N}$ , and the loss function is approximated by  $-1/N_{\text{batch}} \sum_{j=1}^{N_{\text{batch}}} \log q_\theta(\mathbf{x}^{(j)})$  within the batch in each step, where  $N_{\text{batch}}$  is the batch size. Each likelihood  $q_\theta(\mathbf{x}^{(j)})$  is calculated by solving the dynamic system (8) by the fourth order Runge-Kutta scheme.

Once  $q_\theta(\mathbf{x})$  is learned, we define the final product

$$p^{\text{TF}}(\mathbf{x}) := q_\theta(\mathbf{x})$$

that can serve as an approximation to the unknown underlying distribution  $p^*(\mathbf{x})$ . Sampling from  $p^{\text{TF}}(\mathbf{x}) = q_\theta(\mathbf{x})$  is carried out by first sampling from the approximate TT representation  $p^{\text{TT}}(\mathbf{x})$ <sup>1</sup> and then applying the pushforward  $f$  again by numerically integrating (8a). Readers may refer to Figure 2 for the evaluation and sampling procedures for  $q_\theta$ .

**Remark 6** *In the case of normalizing flow, the base distribution chosen as a normal distribution has no information of the target distribution  $p^*$ . Thus, a large neural network is needed so that the flow model is sufficiently expressive to learn the complicated pushforward from the normal distribution to  $p^*$ . However, in our tensorizing flow approach, the base distribution  $p^{\text{TT}}$  chosen as the TT representation is already believed to approximate  $p^*$  well so the flow model here suffices to be close to the identity map, and it is expected to learn a good density approximation  $p^{\text{TF}}$  with a simple and easy-to-train neural network, which may lead to better generalization for our model as well. Furthermore, when the potential function  $\phi_\theta$  in the continuous-time flow model is initialized as a constant function, both the forward and inverse map are obviously the identity at the beginning of training. It means that  $p^{\text{TT}}$  as an initial approximation of  $p^E$  is exploited as priori knowledge, and we are guaranteed to obtain a better density approximation  $p^{\text{TF}}$  than  $p^{\text{TT}}$  through training.*

For this near-identity flow, one may also consider adopting residual flows (He et al., 2016). Several related works (e.g. Gomez et al., 2017; Jacobsen et al., 2018) use some techniques by introducing extra variables to create reversible network architectures based on residual connections. However, compared with several classical flows such as NICE (Dinh et al., 2014), Real NVP (Dinh et al., 2016), MAF (Papamakarios et al., 2017), and Glow (Kingma and Dhariwal, 2018), these networks cannot be inverted analytically, which greatly affects their efficiency and feasibility. Moreover, due to the use of convolutional layers in these networks, the evaluation of the Jacobian determinant in (6) is very expensive and often requires a biased yet still expensive estimate of the log-Jacobian given by the power series for the trace of the matrix logarithm  $\log(\det(I + F)) = \text{tr}(\log(I + F)) = \sum_{k=1}^{\infty} (-1)^{k-1} \text{tr}(F)^k / k$ . Since we are using an ODE-based continuous-time flow model, both the path and the log-Jacobian can be obtained by numerical integration of (8), circumventing the inefficiency aforementioned.

---

1. One may refer to the algorithms by Dolgov et al. (2020) and Novikov et al. (2021) for efficiently sampling from a given TT representation.

Before ending the algorithmic discussion, we provide below a summary of our method.

---

**Algorithm 1** Tensorizing flow
 

---

**Require:** A collection of samples  $\{\mathbf{x}^{(i)}\}_{1 \leq i \leq N}$  independently drawn from an underlying distribution  $p^*(\mathbf{x}) : I^d \rightarrow \mathbb{R}$ ;

1. Construct the approximate TT representation  $p^{\text{TT}}(\mathbf{x})$  from the samples  $\{\mathbf{x}^{(i)}\}_{1 \leq i \leq N}$  following the routine outlined in Section 3.1.2.
  2. Construct a potential function  $\phi_\theta(\mathbf{x})$  parameterized by the neural network  $\theta$ , set  $q(\mathbf{x}, 0) = p^{\text{TT}}(\mathbf{x})$ , and construct the density estimation  $q_\theta(\mathbf{x}) = q(\mathbf{x}, T)$  by applying Runge-Kutta scheme to (8) with stepsize  $\tau$  for  $\lfloor T/\tau \rfloor$  steps;
  3. Train the neural network on the sample set  $\{\mathbf{x}^{(i)}\}_{1 \leq i \leq N}$  w.r.t. loss function (18) and output  $q_\theta(\mathbf{x})$  as the final estimation  $p^{\text{TF}}(\mathbf{x})$  for  $p^*(\mathbf{x})$ .
- 

## 4. Experimental results

We present here several experimental results that illustrate the performance of our algorithm. Under the assumption  $\text{supp}(p) \subset I^d$ , the algorithm is implemented with proper transformation and scaling of the Legendre polynomials for an arbitrary interval  $I$  other than  $[-1, 1]$ , and we will specify the choice of  $I$  for each example below. Gauss-Legendre quadrature is adopted for all numerical integration involved in the construction of the TT representation with  $l$  quadrature points along each dimension.

For the neural network used to parameterize the potential function  $\phi_\theta : \mathbb{R}^d \rightarrow \mathbb{R}$  in the flow model, we adopt a multi-layer perceptron (MLP) structure with an input layer, two hidden layers of  $D$  neurons, and an output layer. The activation functions are chosen as log cosh and the softplus function for the first and second hidden layer, respectively, in order to provide sufficient smoothness for  $\phi_\theta$  as well as  $q_\theta$ . We use the Adam optimizer for the training of the neural network with two parameters: learning rate (LR) and weight decay (WD), and scale the learning rate by a multiplicative factor  $\gamma$  after each epoch, the choices of which are organized in Table 1 in Appendix B. All the experiments are implemented using PyTorch deep learning framework and conducted by a Tesla V100 GPU.

Throughout all the examples in this section, we present the experiment results of our tensorizing flow (TF) algorithm (Algorithm 1) compared with those of normalizing flow (NF), where we use the continuous-time flow model of the same neural network architecture and parameters (see Table 1) as a pushforward from the normal distribution, for the purpose of offering a fair and direct comparison and showcasing the advantage of our approach.

We would also like to point out that the loss (18) satisfies

$$\mathcal{L}(\theta) = -\mathbb{E}_{\mathbf{x} \sim p^E} \log q_\theta(\mathbf{x}) = \text{D}_{\text{KL}} \left( p^E(\cdot) \parallel q_\theta(\cdot) \right) - \mathbb{E}_{\mathbf{x} \sim p^E} \log p^E(\mathbf{x}).$$

Therefore, one should *not* expect the loss to approach zero during the training process.



#### 4.1 Rosenbrock distribution

In this example, we consider the distribution induced by the Rosenbrock function  $v(x)$ , *i.e.*  $p^*(\mathbf{x}) \propto \exp(-v(\mathbf{x})/2)$ , where

$$v(\mathbf{x}) = \sum_{i=1}^{d-1} \left[ c_i^2 x_i^2 + (c_{i+1} x_{i+1} + 5(c_i^2 x_i^2 + 1))^2 \right].$$

Here we set the dimension  $d = 10$ , restrict all  $x_i$  to the finite interval  $I = [-1, 1]$ , and select the scaling factor  $c_i = 2$  for  $1 \leq i \leq d - 2$ ,  $c_{d-1} = 7$ , and  $c_d = 200$ , following the example used by Dolgov et al. (2020). As shown in Figure 6, although the Rosenbrock distribution is designed to be relatively isotropic in the first  $d - 2$  variables, it is concentrated along a curve on the last two dimensions.

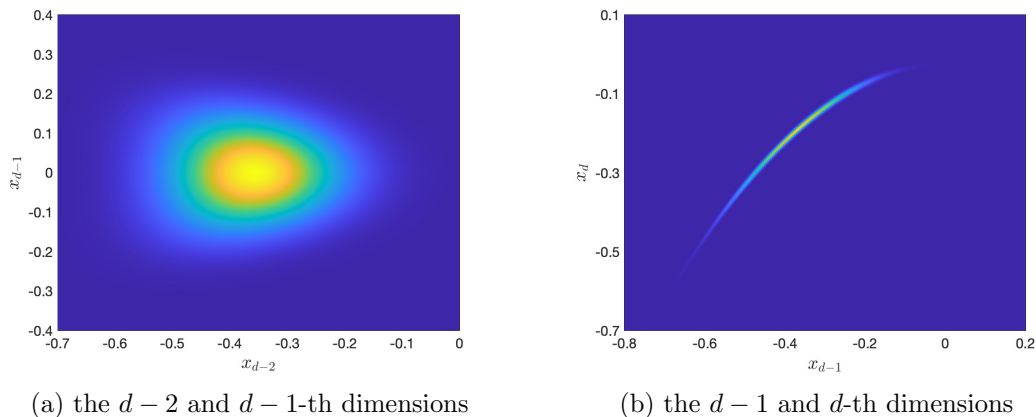


Figure 6: Marginal distributions of the Rosenbrock distribution: a singular structure appears on the last two dimensions.

The experiment results are shown in Figure 7. It can be seen that our algorithm starts with a much lower loss compared to the normalizing flow. This confirms our expectation that the approximate TT representation  $p^{\text{TT}}(\mathbf{x})$  serves as a much better base distribution  $q(\mathbf{x}, 0)$  than the normal distribution in the flow model in terms of both initial and final losses.

Figure 8 and 9 illustrate several samples generated by our method compared with the given samples. It is clear that compared to using a normal distribution as the base distribution, using the approximate TT representation better captures the rough structure of the target distribution. In the work by Dolgov et al. (2020), extra fine grids on the last two dimensions (4 and 32 times finer than the first  $d - 2$  dimensions, respectively) are adopted to deal with the singular tail structure. However, since the empirical distribution is smoothed by kernel density estimation in our approach, no other specific measures to the last two dimensions are required for constructing the approximate TT representation and the subsequent neural network-based flow corrects the estimation automatically.

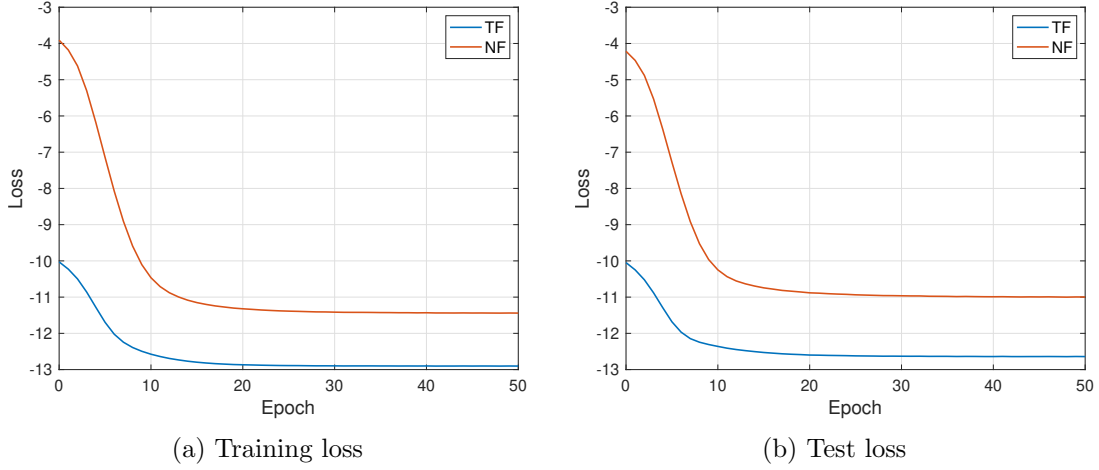


Figure 7: Estimating the Rosenbrock distribution of dimension  $d = 10$  with sample size  $N = 10^5$ : The initial and final loss of TF are both better than those of NF when training with the same neural network architecture and parameters.

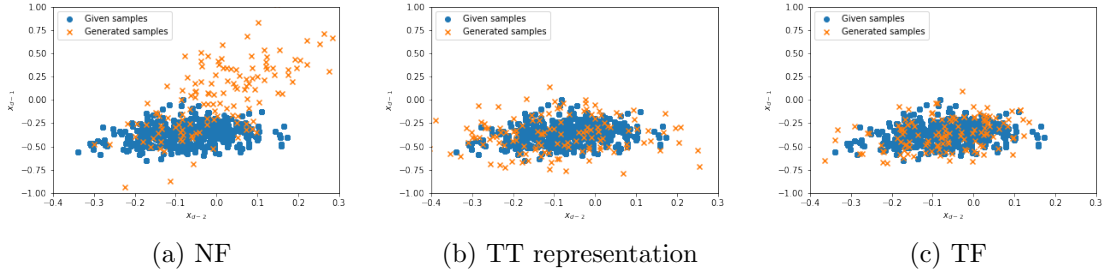


Figure 8: Sampling results projected on the  $d - 2$  and  $d - 1$ -th dimension for Rosenbrock distribution of dimension  $d = 10$ : Samples from tensorizing flow agree better with the original distribution.

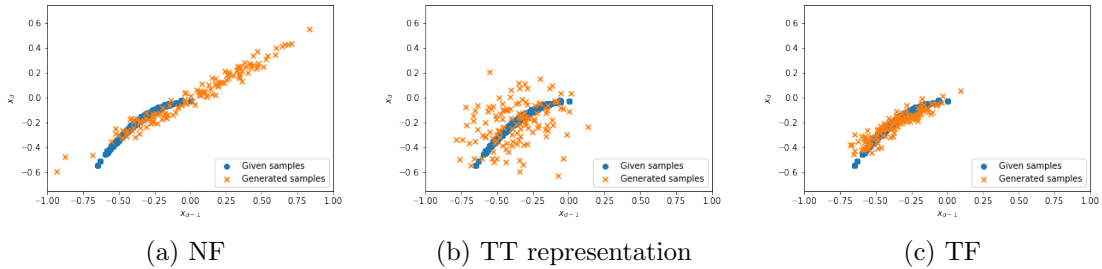


Figure 9: Sampling results projected on the  $d - 1$  and  $d$ -th dimension for Rosenbrock distribution of dimension  $d = 10$ : Tensor-train has limitations in representing the tail structure which in contrast can be learned satisfactorily by TF.

## 4.2 Ginzburg-Landau distribution

The Ginzburg-Landau (GL) theory is a widely-used model for the study of phase transition in statistical mechanics (Hohenberg and Krekhov, 2015). The general Ginzburg-Landau potential defined for a sufficiently smooth function  $x(\mathbf{r}) : \Omega \rightarrow \mathbb{R}$ , where  $\Omega \subset \mathbb{R}^k$  is some domain with suitable boundary conditions, is

$$\mathcal{E}[x(\cdot)] = \int_{\Omega} \left[ \frac{\delta}{2} |\nabla_{\mathbf{r}} x(\mathbf{r})|^2 + \frac{1}{\delta} V(x(\mathbf{r})) \right] d\mathbf{r}, \quad (19)$$

where the potential  $V(x) = (1 - x^2)^2 / 4$ .

### 4.2.1 1D GINZBURG-LANDAU DISTRIBUTION

In the 1-dimensional case of the Ginzburg-Landau potential, we fix the domain  $\Omega = [0, L]$  and discretize the function  $x(\mathbf{r})$  with the vector  $\mathbf{x} = (x_0, \dots, x_{d+1})$  consisting of its values on the uniform grid  $(ih)_{i=0}^{d+1}$  with Dirichlet boundary condition  $x_0 = x_{d+1} = 0$  and grid size  $h = L/(d + 1)$ . Consequently, by using the first-order finite difference scheme and estimating the integral in (19) by the right Riemann sum, the 1D Ginzburg-Landau potential is approximated by

$$E(\mathbf{x}) = \sum_{i=1}^{d+1} \left[ \frac{\delta}{2} \left( \frac{x_i - x_{i-1}}{h} \right)^2 + \frac{1}{4\delta} (1 - x_i^2)^2 \right] \quad (20)$$

and its associated Boltzmann distribution satisfies  $p^*(\mathbf{x}) \propto \exp(-\beta E(\mathbf{x}))$ , where  $\beta$  is the inverse temperature. As mentioned by E et al. (2004), most of the states  $\mathbf{x}$  of interest lie within the range between  $\mathbf{x}_-$  and  $\mathbf{x}_+$ , the two minimizers of the 1D Ginzburg-Landau potential (20) shown in Figure 10. Thus we choose  $I = [-3, 3]$  as the range for each  $x_i$  in the discretization  $\mathbf{x}$ .

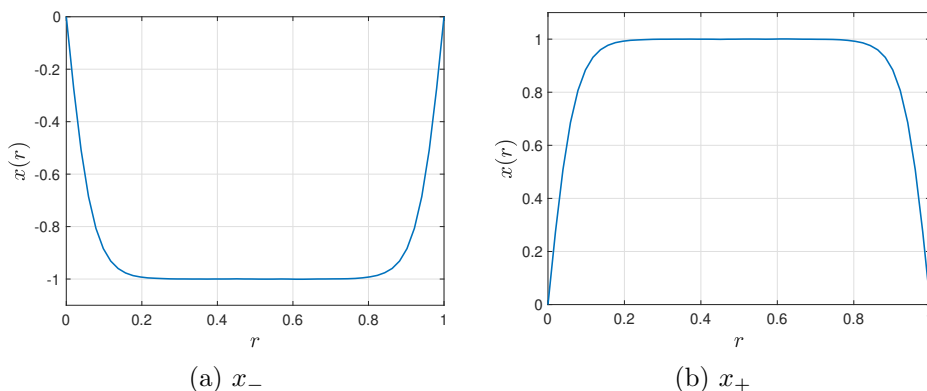


Figure 10: Two local minimizers of the 1D GL potential with  $\delta = 0.05$  and  $L = 1$ .

The results for the case where  $d = 8$ ,  $\beta = 3$ ,  $\delta = 0.5$ , and  $h = 1$  are shown in Figure 11. We can see that as in the previous example, the loss of the tensorizing flow starts lower than normalizing flow, and ends up better than its counterpart.

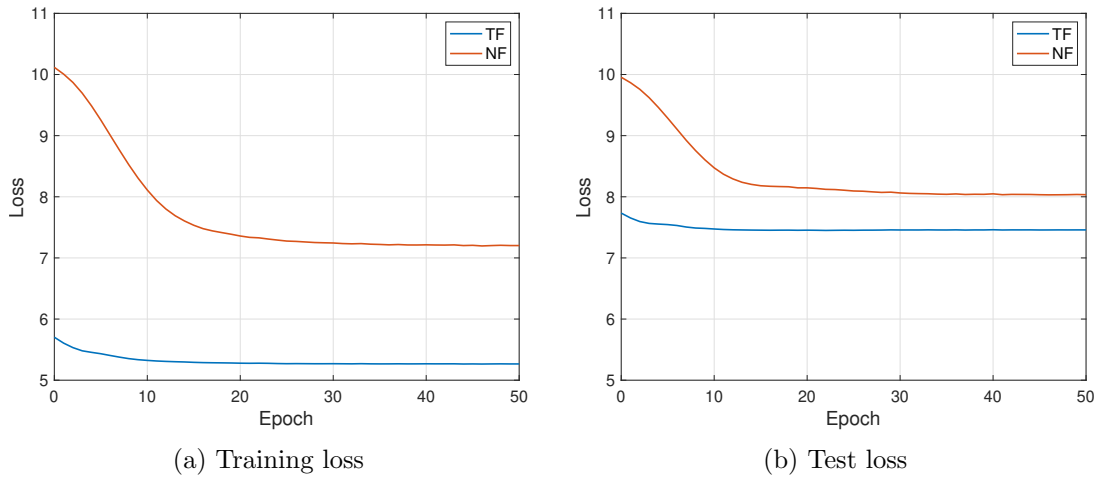


Figure 11: Estimating the 1D GL distribution of dimension  $d = 8$  with sample size  $N = 10^4$ .

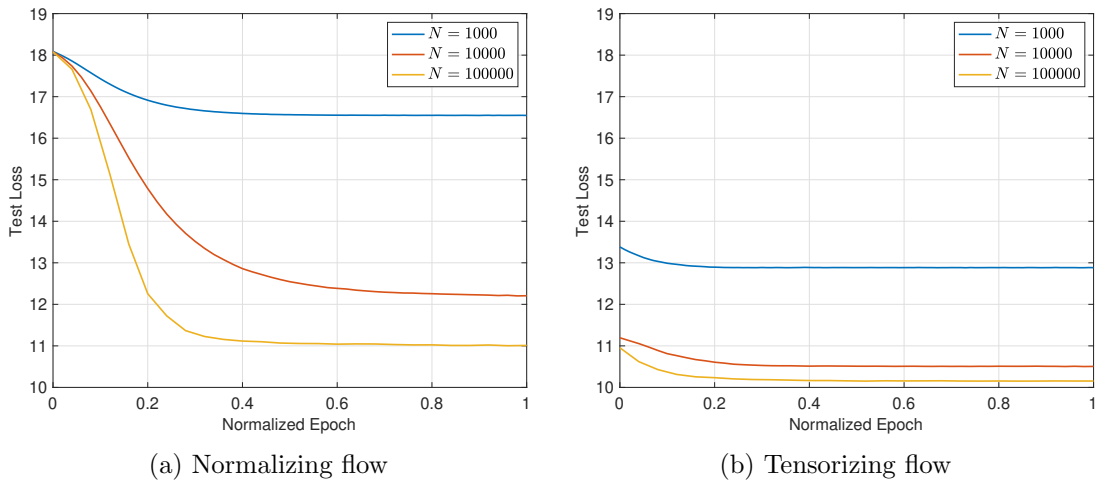


Figure 12: Comparison of test loss for estimating 1D GL distribution of dimension  $d = 16$  with different sample sizes  $N$ : TF yields better results with much fewer samples than NF of the same neural network architecture.

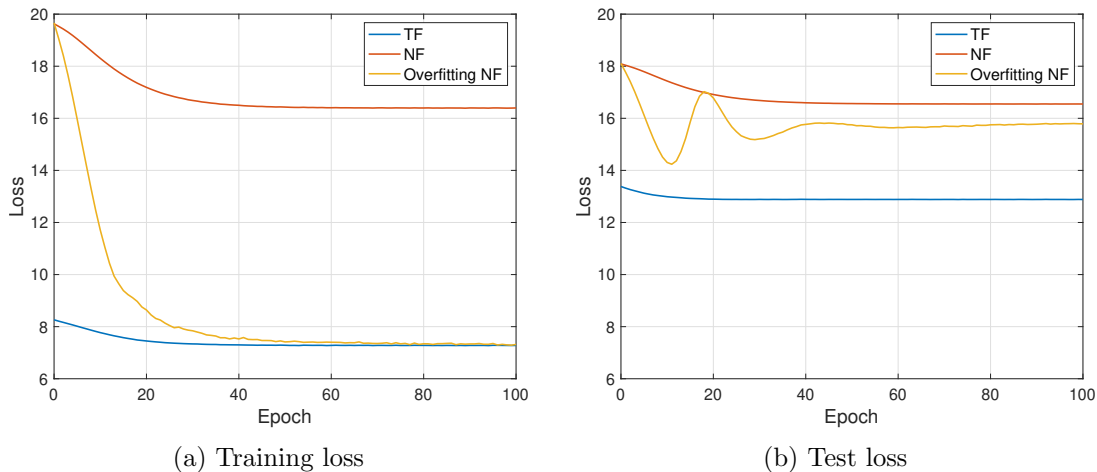


Figure 13: Estimating the 1D GL distribution of dimension  $d = 16$  with sample size  $N = 1000$ : NF with  $10^6$  parameters overfits significantly compared with TF with  $10^4$  parameters.

In order to demonstrate the effect of the sample size on our method, we also perform experiments to the setting  $d = 16$ ,  $\beta = 3$ ,  $\delta = 1$ , and  $h = 1$  with sample sizes  $10^3$ ,  $10^4$ , and  $10^5$ . The training parameters including the number of epochs, learning rate, *etc.*, are adjusted proportionally to offer a fair comparison between these experiments (see Table 1). The results are shown in Figure 12, where the horizontal axis is the normalized epoch, *i.e.* epoch divided by the total number of epochs, and the vertical axis is the test loss computed using a common test set of size  $5 \times 10^3$ . As the performance of the normalizing flow keeps improving when the sample size increases, a larger sample set also yields a better TT representation  $p^{\text{TT}}$  to start with and eventually a better density estimation  $p^{\text{TF}}$  after training. Also, Figure 12 indicates that our method produces a better density estimation with  $10^4$  samples than that with  $10^5$  samples by normalizing flow, which corroborates the efficiency of our method in the sense of samples required for reaching certain accuracy of the density estimation.

In Figure 13, we present another example with  $d = 16$ ,  $\beta = 3$ ,  $\delta = 1$ ,  $h = 1$ , and  $N = 10^3$  trying to understand why normalizing flow cannot achieve the same test loss as tensorizing flow. With the same architecture, indeed normalizing flow has higher training and test losses than tensorizing flow (see the red curves in Figure 13). In order to improve the training loss of normalizing flow, we use a relatively overparameterized NN for normalizing flow (see the corresponding parameters in Table 1) so that its training loss matches with that of the tensorizing flow (see the yellow curve in Figure 13a). It is clear that with a matching training loss, normalizing flow overfits significantly (see the yellow curve in Figure 13b), demonstrating that tensorizing flow provides much better generalization and is not prone to overfit, since it only uses a relatively small and less expressive neural network.

#### 4.2.2 2D GINZBURG-LANDAU DISTRIBUTION

In the 2-dimensional case of the Ginzburg-Landau potential, we fix the domain  $\Omega = [0, L]^2$  and discretize the function  $x(\mathbf{r})$  by the matrix  $\mathbf{x} = (x_{i,j})_{i,j=1}^{\sqrt{d}}$  where  $x_{i,j}$  represents its

value at the grid point  $((i-1)h, (j-1)h)$  with grid size  $h = L/(\sqrt{d}-1)$ . With a similar discretization procedure as in the 1-dimensional case, the probability density function of the 2D Ginzburg-Landau distribution satisfies  $p^*(\mathbf{x}) \propto \exp(-\beta E(\mathbf{x}))$ , where

$$E(\mathbf{x}) = \sum_{i=1}^{\sqrt{d}} \sum_{j=1}^{\sqrt{d}} \left[ \frac{\delta}{2} \left( \left( \frac{x_{i,j} - x_{i-1,j}}{h} \right)^2 + \left( \frac{x_{i,j} - x_{i,j-1}}{h} \right)^2 \right) + \frac{1}{4\delta} (1 - x_{i,j}^2)^2 \right] \quad (21)$$

and the periodic boundary condition is adopted, *i.e.*  $x_{0,j} = x_{\sqrt{d},j}$  for  $1 \leq j \leq \sqrt{d}$  and  $x_{i,0} = x_{i,\sqrt{d}}$  for  $1 \leq i \leq \sqrt{d}$ , as shown in Figure 14.

Unlike the 1D Ginzburg-Landau model, the 2D Ginzburg-Landau is not Markovian. In order to obtain an approximate TT representation using the algorithm proposed in Section 3.1, we adopt the “snake ordering” when vectorizing the matrix  $\mathbf{x}$  in the order demonstrated by the red arrow path in Figure 14 to exploit the Markovian structure of (21) to the largest extent.

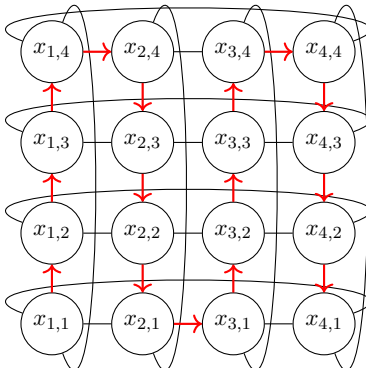


Figure 14: Periodic boundary condition of the 2D Ginzburg-Landau distribution and the “snake ordering” of the matrix variable  $\mathbf{x}$  of dimension  $d = 4 \times 4$ : pairs of variables with energy functions between them are connected by black lines and the vectorization of  $\mathbf{x}$  is along the order indicated by the red arrow path.

In our example, we set the dimension  $d = 4 \times 4$ ,  $\beta = 1.5$ ,  $\delta = 1$ ,  $h = 1$ . The range of each  $x_{i,j}$  is also assumed to be within  $I = [-3, 3]$ . The experiment results of this example are shown in Figure 15, which further confirms the effectiveness of our algorithm over either normalizing flow or the TT representation when dealing with more complicated non-Markovian distributions.

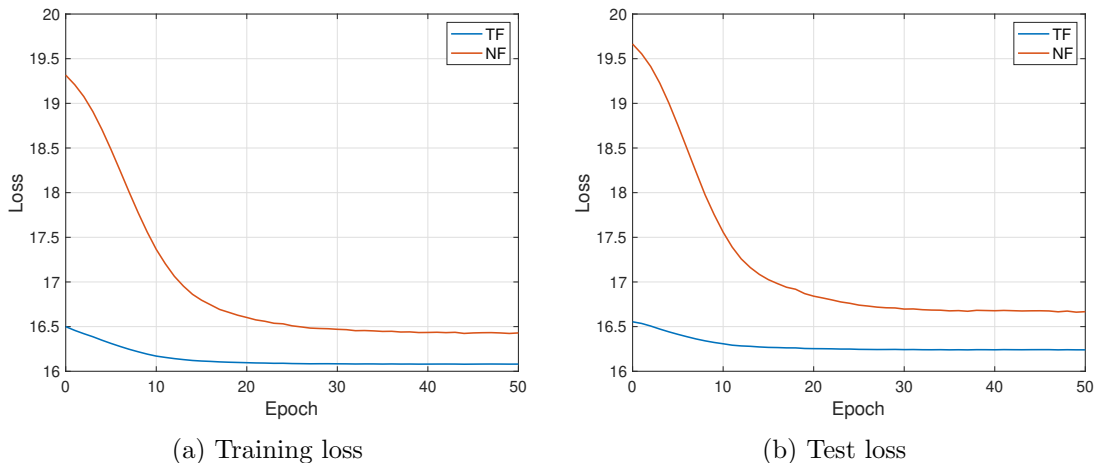


Figure 15: Estimating the 2D Ginzburg-Landau distribution of dimension  $d = 4 \times 4$  with sample size  $N = 10^4$ : TF learns a complicated non-Markovian density.

## 5. Discussions

We proposed a generative model for high-dimensional density estimation from a finite collection of samples. Using a sketching technique, we construct an approximate tensor-train representation efficiently. When constructing the tensor-train, we adopt kernel density estimation for estimating the required low-dimensional marginals. Starting from the tensor-train representation as the base distribution, we perform the continuous-time flow model to further refine our density estimation, featuring a potential function parameterized by a neural network and fast calculation of both the forward and inverse map by Runge-Kutta scheme.

Several experiments demonstrate that our method evidently outperforms normalizing flow of similar architectures and is capable of dealing with distributions of certain singularity as well as non-Markovian models, for which traditional tensor-train methods may run into difficulties. Due to the near-identity nature of the tensorizing flow, a relatively simple neural network suffices for the flow model, which is much easier to train and less prone to overfitting compared with normalizing flow.

However, our method is still confined to the presumed Markovian structure of the distribution and future research may focus on designing a more adaptive scheme for non-Markovian models with more complicated graph structure. Furthermore, although the Legendre polynomials are used as the expansion basis in this work, our method is open to other expansion basis, including the Chebyshev polynomials and the Fourier basis.

## Acknowledgments and Disclosure of Funding

Yinuo Ren and Lexing Ying are partially supported by National Science Foundation under Award No. DMS-2011699. Hongli Zhao and Yuehaw Khoo are partially supported by National Science Foundation under Award No. DMS-2111563. Yuehaw Khoo is partially supported by U.S. Department of Energy, Office of Science under Award No. DE-SC0022232.

### A. Proof of Proposition 3

In this appendix we prove the Proposition 3 from Section 3.1:

**Proof of Proposition 3.** For  $2 \leq k \leq d$ , it suffices for us to consider the  $k$ -th equation in (10):

$$\sum_{\alpha_{k-1}=1}^{r_{k-1}} \Phi_{k-1}(x_{1:k-1}; \alpha_{k-1}) G_k(\alpha_{k-1}; x_k, \alpha_k) = \Phi_k(x_{1:k-1}; x_k, \alpha_k). \quad (22)$$

By Definition 1, there exist orthonormal right singular vectors

$$\{\Psi_{k-1}(\alpha_{k-1}; x_{k:d})\}_{1 \leq \alpha_{k-1} \leq r_{k-1}} \subset L^2(I^{d-k+1})$$

of  $p(x_{1:k-1}; x_{k:d})$  and

$$\{\Psi_k(\alpha_k; x_{k+1:d})\}_{1 \leq \alpha_k \leq r_k} \subset L^2(I^{d-k})$$

of  $p(x_{1:k}; x_{k+1:d})$ , and corresponding singular values  $\sigma_{k-1}(1) \geq \dots \geq \sigma_{k-1}(r_{k-1})$  and  $\sigma_k(1) \geq \dots \geq \sigma_k(r_k)$ , satisfying

$$p(x_{1:k-1}; x_{k:d}) = \sum_{\alpha_{k-1}=1}^{r_{k-1}} \sigma_{k-1}(\alpha_{k-1}) \Phi_{k-1}(x_{1:k-1}; \alpha_{k-1}) \Psi_{k-1}(\alpha_{k-1}; x_{k:d}), \quad (23)$$

and

$$p(x_{1:k}; x_{k+1:d}) = \sum_{\alpha_k=1}^{r_k} \sigma_k(\alpha_k) \Phi_k(x_{1:k}; \alpha_k) \Psi_k(\alpha_k; x_{k+1:d}).$$

Define  $\Xi_k(x_{k+1:d}; \alpha_k) = \sigma_k(\alpha_k)^{-1} \Psi_k(\alpha_k; x_{k+1:d})$ . It is easy to check that

$$\begin{aligned} & \int_{I^{d-k}} p(x_{1:k}; x_{k+1:d}) \Xi_k(x_{k+1:d}; \alpha_k) dx_{k+1:d} \\ &= \int_{I^{d-k}} \sum_{\alpha'_k=1}^{r_k} \sigma_k(\alpha'_k) \sigma_k(\alpha_k)^{-1} \Phi_k(x_{1:k}; \alpha'_k) \Psi_k(\alpha'_k; x_{k+1:d}) \Psi_k(\alpha_k; x_{k+1:d}) dx_{k+1:d} \\ &= \Phi_k(x_{1:k}; \alpha_k). \end{aligned}$$

Therefore, by contracting  $\Xi_k(x_{k+1:d}; \alpha_k)$  to both sides of (23), we have

$$\begin{aligned} \Phi_k(x_{1:k}; \alpha_k) &= \int_{I^{d-k}} p(x_{1:k-1}; x_{k:d}) \Xi_k(x_{k+1:d}; \alpha_k) dx_{k+1:d} \\ &= \sum_{\alpha_{k-1}=1}^{r_{k-1}} \sigma_{k-1}(\alpha_{k-1}) \Phi_{k-1}(x_{1:k-1}; \alpha_{k-1}) \int_{I^{d-k}} \Psi_{k-1}(\alpha_{k-1}; x_{k:d}) \Xi_k(x_{k+1:d}; \alpha_k) dx_{k+1:d}, \end{aligned}$$

and consequently

$$G_k(\alpha_{k-1}; x_k, \alpha_k) = \sigma_{k-1}(\alpha_{k-1}) \int_{I^{d-k}} \Psi_{k-1}(\alpha_{k-1}; x_{k:d}) \Xi_k(x_{k+1:d}; \alpha_k) dx_{k+1:d}$$

solves the equation (22).

The uniqueness of the solution is guaranteed by the orthogonality of the functions  $\{\Psi_{k-1}(\alpha_{k-1}; x_{k:d})\}_{1 \leq \alpha_{k-1} \leq r_{k-1}}$  by definition. Once  $G_k$  are ready, it is easy to check the validity of (11) by plugging the CDE in (10) one into the next successively.



## B. Hyperparameters

In this section, we present the hyperparameters of our tensorizing flow algorithm used for each examples in Section 4. For simplicity, we choose the internal ranks  $r_k = 2$  for  $1 \leq k \leq d - 1$ , and the number of quadrature points  $l = 20$  for all numerical integrations involved. We set the time horizon  $T = 0.2$  with stepsize  $\tau = 0.01$  in the flow model. We generate  $N/2$  samples separately from the training samples as the test samples. The rest of hyperparameters are organized in Table 1.

Example	Instance	$N$	$M$	$N_{\text{batch}}$	$D$	LR	WD	$\gamma$
<b>Rosenbrock(Figure 7)</b>	<b>TF/NF</b>	1e+5	30	5e+3	64	5e-4	2e-3	0.9
<b>1D GL(Figure 11)</b>	<b>TF/NF</b>	1e+4	25	5e+3	128	5e-3	1e-3	0.9
<b>1D GL(Figure 12)</b>	<b>TF/NF</b>	1e+3	25	1e+3	128	5e-3	1e-3	0.9
		1e+4	25	5e+3	128	5e-3	1e-3	0.9
		1e+5	25	5e+3	128	2e-3	1e-3	0.85
<b>1D GL(Figure 13)</b>	<b>TF/NF</b>	1e+3	25	1e+3	128	5e-3	1e-3	0.9
	<b>Overfitting NF</b>	1e+3	25	1e+3	1024	2e-3	1e-3	0.9
<b>2D GL(Figure 15)</b>	<b>TF/NF</b>	1e+4	25	5e+3	128	5e-3	1e-3	0.9

Table 1: Hyperparameters used in the examples

## References

- M. Bachmayr, R. Schneider, and A. Uschmajew. Tensor networks and hierarchical tensors for the solution of high-dimensional partial differential equations. *Foundations of Computational Mathematics*, 16(6):1423–1472, 2016.
- A. Baiardi and M. Reiher. The density matrix renormalization group in chemistry and molecular physics: Recent developments and new challenges. *The Journal of Chemical Physics*, 152(4):040903, 2020.
- G. K. Batchelor. *An introduction to fluid dynamics*. Cambridge university press, 2000.
- J. Behrmann, W. Grathwohl, R. T. Chen, D. Duvenaud, and J.-H. Jacobsen. Invertible residual networks. In *International Conference on Machine Learning*, pages 573–582. PMLR, 2019.
- Y. Bengio, R. Ducharme, and P. Vincent. A neural probabilistic language model. *Advances in neural information processing systems*, 13, 2000.
- C. M. Bishop and N. M. Nasrabadi. *Pattern recognition and machine learning*, volume 4. Springer, 2006.
- D. M. Blei, A. Kucukelbir, and J. D. McAuliffe. Variational inference: A review for statisticians. *Journal of the American statistical Association*, 112(518):859–877, 2017.

- S. Bond-Taylor, A. Leach, Y. Long, and C. G. Willcocks. Deep generative modelling: A comparative review of vaes, gans, normalizing flows, energy-based and autoregressive models. *arXiv preprint arXiv:2103.04922*, 2021.
- T.-D. Bradley, E. M. Stoudenmire, and J. Terilla. Modeling sequences with quantum states: a look under the hood. *Machine Learning: Science and Technology*, 1(3):035008, 2020.
- F. G. Brandao and M. Horodecki. Exponential decay of correlations implies area law. *Communications in mathematical physics*, 333(2):761–798, 2015.
- G. K.-L. Chan and S. Sharma. The density matrix renormalization group in quantum chemistry. *Annual review of physical chemistry*, 62(1):465–481, 2011.
- C. Chen, C. Li, L. Chen, W. Wang, Y. Pu, and L. C. Duke. Continuous-time flows for efficient inference and density estimation. In *International Conference on Machine Learning*, pages 824–833. PMLR, 2018a.
- R. T. Chen, Y. Rubanova, J. Bettencourt, and D. K. Duvenaud. Neural ordinary differential equations. *Advances in neural information processing systems*, 31, 2018b.
- S. Cheng, L. Wang, T. Xiang, and P. Zhang. Tree tensor networks for generative modeling. *Physical Review B*, 99(15):155131, 2019.
- A. Cichocki, R. Zdunek, A. H. Phan, and S.-i. Amari. *Nonnegative matrix and tensor factorizations: applications to exploratory multi-way data analysis and blind source separation*. John Wiley & Sons, 2009.
- L. De Lathauwer, B. De Moor, and J. Vandewalle. A multilinear singular value decomposition. *SIAM journal on Matrix Analysis and Applications*, 21(4):1253–1278, 2000a.
- L. De Lathauwer, B. De Moor, and J. Vandewalle. On the best rank-1 and rank- $(r_1, r_2, \dots, r_n)$  approximation of higher-order tensors. *SIAM journal on Matrix Analysis and Applications*, 21(4):1324–1342, 2000b.
- L. Dinh, D. Krueger, and Y. Bengio. Nice: Non-linear independent components estimation. *arXiv preprint arXiv:1410.8516*, 2014.
- L. Dinh, J. Sohl-Dickstein, and S. Bengio. Density estimation using real nvp. *arXiv preprint arXiv:1605.08803*, 2016.
- S. Dolgov, K. Anaya-Izquierdo, C. Fox, and R. Scheichl. Approximation and sampling of multivariate probability distributions in the tensor train decomposition. *Statistics and Computing*, 30(3):603–625, 2020.
- S. V. Dolgov, B. N. Khoromskij, I. V. Oseledets, and D. V. Savostyanov. Computation of extreme eigenvalues in higher dimensions using block tensor train format. *Computer Physics Communications*, 185(4):1207–1216, 2014.
- E. Dupont, A. Doucet, and Y. W. Teh. Augmented neural odes. *Advances in Neural Information Processing Systems*, 32, 2019.

- C. Durkan, A. Bekasov, I. Murray, and G. Papamakarios. Cubic-spline flows. *arXiv preprint arXiv:1906.02145*, 2019a.
- C. Durkan, A. Bekasov, I. Murray, and G. Papamakarios. Neural spline flows. *Advances in neural information processing systems*, 32, 2019b.
- W. E. W. Ren, and E. Vanden-Eijnden. Minimum action method for the study of rare events. *Communications on pure and applied mathematics*, 57(5):637–656, 2004.
- M. Germain, K. Gregor, I. Murray, and H. Larochelle. Made: Masked autoencoder for distribution estimation. In *International conference on machine learning*, pages 881–889. PMLR, 2015.
- A. N. Gomez, M. Ren, R. Urtasun, and R. B. Grosse. The reversible residual network: Backpropagation without storing activations. *Advances in neural information processing systems*, 30, 2017.
- I. Goodfellow, J. Pouget-Abadie, M. Mirza, B. Xu, D. Warde-Farley, S. Ozair, A. Courville, and Y. Bengio. Generative adversarial nets. *Advances in neural information processing systems*, 27, 2014.
- L. Grasedyck. Hierarchical singular value decomposition of tensors. *SIAM journal on matrix analysis and applications*, 31(4):2029–2054, 2010.
- W. Grathwohl, R. T. Chen, J. Bettencourt, I. Sutskever, and D. Duvenaud. Ffjord: Free-form continuous dynamics for scalable reversible generative models. *arXiv preprint arXiv:1810.01367*, 2018.
- Z.-Y. Han, J. Wang, H. Fan, L. Wang, and P. Zhang. Unsupervised generative modeling using matrix product states. *Physical Review X*, 8(3):031012, 2018.
- K. He, X. Zhang, S. Ren, and J. Sun. Deep residual learning for image recognition. In *Proceedings of the IEEE conference on computer vision and pattern recognition*, pages 770–778, 2016.
- G. E. Hinton. Training products of experts by minimizing contrastive divergence. *Neural computation*, 14(8):1771–1800, 2002.
- G. E. Hinton and T. J. Sejnowski. Optimal perceptual inference. In *Proceedings of the IEEE conference on Computer Vision and Pattern Recognition*, volume 448, pages 448–453. Citeseer, 1983.
- M. D. Hoffman, D. M. Blei, C. Wang, and J. Paisley. Stochastic variational inference. *Journal of Machine Learning Research*, 2013.
- P. Hohenberg and A. Krekhov. An introduction to the ginzburg-landau theory of phase transitions and nonequilibrium patterns. *Physics Reports*, 572:1–42, 2015.
- Y. Hur, J. G. Hoskins, M. Lindsey, E. Stoudenmire, and Y. Khoo. Generative modeling via tensor train sketching. *arXiv preprint arXiv:2202.11788*, 2022.

- J.-H. Jacobsen, A. Smeulders, and E. Oyallon. i-revnet: Deep invertible networks. *arXiv preprint arXiv:1802.07088*, 2018.
- Y. Khoo, M. Lindsey, and H. Zhao. Tensorizing flows: a tool for variational inference. *In preparation*, 2022.
- D. P. Kingma and P. Dhariwal. Glow: Generative flow with invertible 1x1 convolutions. *Advances in neural information processing systems*, 31, 2018.
- D. P. Kingma and M. Welling. Auto-encoding variational bayes. *arXiv preprint arXiv:1312.6114*, 2013.
- D. P. Kingma, T. Salimans, R. Jozefowicz, X. Chen, I. Sutskever, and M. Welling. Improved variational inference with inverse autoregressive flow. *Advances in neural information processing systems*, 29, 2016.
- I. Kobyzev, S. J. Prince, and M. A. Brubaker. Normalizing flows: An introduction and review of current methods. *IEEE transactions on pattern analysis and machine intelligence*, 43(11):3964–3979, 2020.
- D. Kressner and A. Uschmajew. On low-rank approximability of solutions to high-dimensional operator equations and eigenvalue problems. *Linear Algebra and its Applications*, 493:556–572, 2016.
- D. Kressner, B. Vandereycken, and R. Voorhaar. Streaming tensor train approximation. *arXiv preprint arXiv:2208.02600*, 2022.
- H. Larochelle and I. Murray. The neural autoregressive distribution estimator. In *Proceedings of the fourteenth international conference on artificial intelligence and statistics*, pages 29–37. JMLR Workshop and Conference Proceedings, 2011.
- Y. Miao, L. Yu, and P. Blunsom. Neural variational inference for text processing. In *International conference on machine learning*, pages 1727–1736. PMLR, 2016.
- A. Mnih and K. Gregor. Neural variational inference and learning in belief networks. In *International Conference on Machine Learning*, pages 1791–1799. PMLR, 2014.
- G. S. Novikov, M. E. Panov, and I. V. Oseledets. Tensor-train density estimation. In *Uncertainty in Artificial Intelligence*, pages 1321–1331. PMLR, 2021.
- I. Oseledets and E. Tyrtysnikov. Tt-cross approximation for multidimensional arrays. *Linear Algebra and its Applications*, 432(1):70–88, 2010.
- I. V. Oseledets. Tensor-train decomposition. *SIAM Journal on Scientific Computing*, 33(5):2295–2317, 2011.
- G. Papamakarios, T. Pavlakou, and I. Murray. Masked autoregressive flow for density estimation. *Advances in neural information processing systems*, 30, 2017.
- R. Penrose. Applications of negative dimensional tensors. *Combinatorial mathematics and its applications*, 1:221–244, 1971.

- D. Perez-Garcia, F. Verstraete, M. M. Wolf, and J. I. Cirac. Matrix product state representations. *arXiv preprint quant-ph/0608197*, 2006.
- R. Ranganath, S. Gerrish, and D. Blei. Black box variational inference. In *Artificial intelligence and statistics*, pages 814–822. PMLR, 2014.
- D. Rezende and S. Mohamed. Variational inference with normalizing flows. In *International conference on machine learning*, pages 1530–1538. PMLR, 2015.
- D. J. Rezende, S. Mohamed, and D. Wierstra. Stochastic backpropagation and approximate inference in deep generative models. In *International conference on machine learning*, pages 1278–1286. PMLR, 2014.
- D. Savostyanov and I. Oseledets. Fast adaptive interpolation of multi-dimensional arrays in tensor train format. In *The 2011 International Workshop on Multidimensional (nD) Systems*, pages 1–8. IEEE, 2011.
- J. Schmidhuber. Generative adversarial networks are special cases of artificial curiosity (1990) and also closely related to predictability minimization (1991). *Neural Networks*, 127:58–66, 2020.
- T. Shi, M. Ruth, and A. Townsend. Parallel algorithms for computing the tensor-train decomposition. *arXiv preprint arXiv:2111.10448*, 2021.
- E. M. Stein and R. Shakarchi. *Real analysis: measure theory, integration, and Hilbert spaces*. Princeton University Press, 2009.
- M. Steinlechner. Riemannian optimization for high-dimensional tensor completion. *SIAM Journal on Scientific Computing*, 38(5):S461–S484, 2016.
- E. G. Tabak and E. Vanden-Eijnden. Density estimation by dual ascent of the log-likelihood. *Communications in Mathematical Sciences*, 8(1):217–233, 2010.
- X. Tang, Y. Hur, Y. Khoo, and L. Ying. Generative modeling via tree tensor network states. *arXiv preprint arXiv:2209.01341*, 2022.
- B. Tzen and M. Raginsky. Neural stochastic differential equations: Deep latent gaussian models in the diffusion limit. *arXiv preprint arXiv:1905.09883*, 2019.
- T. Vieijra, L. Vanderstraeten, and F. Verstraete. Generative modeling with projected entangled-pair states. *arXiv preprint arXiv:2202.08177*, 2022.
- W. Wang, V. Aggarwal, and S. Aeron. Tensor train neighborhood preserving embedding. *IEEE Transactions on Signal Processing*, 66(10):2724–2732, 2018.
- S. R. White. Density-matrix algorithms for quantum renormalization groups. *Physical review b*, 48(14):10345, 1993.
- N. Young. *An introduction to Hilbert space*. Cambridge university press, 1988.
- L. Zhang, L. Wang, et al. Monge-ampère flow for generative modeling. *arXiv preprint arXiv:1809.10188*, 2018.